

UCSF

UC San Francisco Previously Published Works

Title

Model of biologically active apolipoprotein E bound to dipalmitoylphosphatidylcholine

Permalink

<https://escholarship.org/uc/item/3wm776n4>

Journal

Journal of Biological Chemistry, 281(2)

ISSN

0021-9258

Authors

Peters-Libeu, C A
Newhouse, Y
Hatters, D M
[et al.](#)

Publication Date

2006

Peer reviewed

Model of biologically active apolipoprotein E bound to dipalmitoylphosphatidylcholine*

Clare A. Peters-Libeuf§, Yvonne Newhouse§, Danny M. Hatters§, and Karl H. Weisgraber§¶**

From the §Gladstone Institute of Cardiovascular Disease and §Gladstone Institute of Neurological Disease, 1650 Owens Street, San Francisco, California 94158, and the ¶Department of Pathology and Cardiovascular Research Institute, University of California, San Francisco, California 94143

Apolipoprotein (apo) E plays a critical role in cholesterol transport, through high-affinity binding to the low density lipoprotein receptor. This interaction requires apoE to be associated with a lipoprotein particle. To determine the structure of biologically active apoE on a lipoprotein particle, we crystallized dipalmitoylphosphatidylcholine particles containing two apoE molecules and determined the molecular envelope of apoE at 10 Å resolution. On the basis of the molecular envelope and supporting biochemical evidence, we propose a model in which each apoE molecule is folded into a helical hairpin with the binding region for the low density lipoprotein receptor at its apex.

Lipoproteins, the major transport vehicles for distribution of triglyceride and cholesterol throughout the body, are divided into different classes based on their apolipoprotein and lipid contents. Although lipoprotein particles have been extensively studied by electron microscopy, neutron diffraction, and x-ray diffraction (for review, see Ref. (1), the resolution has not been sufficient to visualize the molecular envelope of individual proteins on the surface of the particle.

Lipoproteins containing apolipoprotein (apo)¹ E serve critical functions in plasma cholesterol and triglyceride metabolism and in the transport and redistribution of lipids among various cells, tissues, and organs (2). ApoE also plays a major role in neurobiology (3). Key to many of these functions is the high-affinity binding of apoE-containing lipoproteins to the low density lipoprotein (LDL) receptor (LDLR) and other members of the LDLR family. The three common isoforms (apoE2, apoE3, and apoE4) exhibit isoform-specific effects in both cardiovascular and neurodegenerative disease. For example, apoE4 is a major susceptibility factor for Alzheimer's disease (4–6) and other forms of neurodegeneration (7–10) and for cardiovascular disease (11, 12).

In the lipid-free state, human apoE (299 residues) has two independently folded structural domains: a

22-kDa N-terminal domain (residues 1–191) containing the LDLR-binding region (residues 140–160 and 172) and a 10-kDa C-terminal domain (residues 216–299) containing the major lipoprotein-binding elements (13, 14). The structure of the C-terminal domain is unknown but predicted to be α -helical (15–17), and the structure of the lipid-free N-terminal domain is a four-helix bundle containing antiparallel α -helices (18). The residues implicated in LDLR binding are surface accessible in the crystal structure; however, until it is associated with lipid, apoE does not display high-affinity binding to the LDLR (19). Since the N-terminal four-helix bundle unfolds and then refolds during lipid binding (20), the final conformation of receptor-active apoE in the lipid-bound state is likely to be dramatically different from that of lipid-free apoE.

To determine how binding to a lipoprotein particle activates apoE's LDLR binding site, we crystallized apoE4 bound to dipalmitoylphosphatidylcholine (DPPC). Here we present an x-ray model of lipid-bound apoE4 at 10 Å resolution.

EXPERIMENTAL PROCEDURES

Production and Crystallization of ApoE4•DPPC Particles—Recombinant apoE4 was expressed and purified as described (21). The apoE4•DPPC particles were produced by modification of the method of Jonas (22) (as described in (23)). Crystals were obtained with the hanging drop method from a mixture of 24% PEG 1000, 20 mM sodium acetate, pH 5.8, and apoE4•DPPC (~2 mg/ml) containing 1% heptanetriol.

Data Collection and Processing—For cryoprotection, apoE4•DPPC crystals were treated with 28% PEG 1000, 20 mM sodium acetate, pH 5.8, 1% heptanetriol, and 15% ethylene glycol. Data were collected at beam lines 8.2.1, 8.2.2 and 8.3.1 at the Advanced Light Source with 1.072 Å x-rays. Data were processed with XDS (24), and the relevant statistics are summarized in Table I and in (23). The space group of the crystals is $P2_1$ with cell constants of $a = 99$ Å, $b = 111$ Å, $c = 79$ Å, and $\beta = 113^\circ$.

Calculation of Radial Intensity—For each crystal, a series of 0.25° oscillation photos was collected every 10° with an ADSC Q315 detector. Sample images corrected for background scattering from the cryoprotectant are included in the Supplementary Information. After data collection, the crystal was removed from its fiber loop. The loop was filled with cryoprotectant, and a second set of images was collected for background subtraction.

The average radial intensity for each image was calculated with FIT2D v6.0 (25). For the low-resolution calculation, a mask for each image was constructed to eliminate pixels corresponding to the Bragg peaks. For the high-resolution calculation, all pixels below the average diffuse scattering intensity outside the arcs were eliminated to better estimate the average intensity of the arcs. To correct for absorption effects, each radial intensity curve was scaled to the radial intensity curve at 0° , using a single scale factor determined by least-squares fitting. Because the images from the cryoprotectant-filled loop showed little variation, the final radial intensity curve for that loop was calculated as the average of the individual radial intensity curves at each orientation. This curve was also scaled to the radial intensity curve from the crystal at 0° . The plotted intensity per pixel is the difference between the scaled radial intensity curve for each image and the final average radial intensity curve for the loop filled with cryoprotectant.

Solution by Molecular Replacement—Belt-like molecular replacement search models were generated by placing pseudoatoms on vertices of a cubic grid. All points that fit within the molecular envelope were accepted into the model and entered into MOLREP (26) as a series of alpha carbons. The molecular replacement solution was independent of the grid spacing between 3.0 and 1.25 Å.

In addition to grid spacing, five parameters of the molecular surface were varied: the outer radius, height, and width of the belt, the angle of completeness, and the eccentricity. The angle of completeness describes the angular extent of the belt and would be 180° for a half belt and 360° for a complete belt. The eccentricity is the ratio of the radii of an ellipse. A perfect circle has an eccentricity of 1.0. The outer radius was varied between 20 Å and 80 Å. The width and the height were varied between 2 and 40 Å. The angle of completeness was varied between 90° and 360° and the eccentricity between 0.5 and 2.0. The radius was varied in increments of 1.0 Å, while the angle of

completeness was varied in steps of 2° , and the eccentricity in steps of 0.05 within a 20% range of their peak values. Outside of this range, increments of 5.0 Å, 10° , and 0.125 were used for the radius, angle of completeness, and eccentricity. The height and the width were varied in increments of 1.0 Å.

Calculation of the Predicted Diffuse Scattering—To interpret the diffuse scattering observed from the apoE•DPPC particles, model particles were constructed by placing pseudoatoms with the appropriate spacing within candidate shapes of the particle. For example, a disk-shaped particle was simulated as two parallel planes of phosphate atoms filled with carbon atoms oriented so that the carbon atoms have a mean 4.2 Å spacing in planes parallel to the planes of the phosphate atoms. Although this model is relatively crude and doesn't provide a complete description of the diffuse scattering expected from a disk-shaped particle, it is sufficient to determine the expected position of the diffuse scattering peaks associated with the phosphate atoms and the 4.2 Å spacing between the carbon atoms.

The diffuse scattering from the phosphate atoms of the spheroidal particle was simulated by filling in phosphate atoms at a radius of 30 Å from the center of the particle. Carbon atoms were placed randomly within the sphere.

Each model was translated to the center of the molecular replacement solution, and then the crystallographically related molecule was generated with the $P2_1$ screw axis. The Fourier transform of each unit cell was calculated with the SFALL program from CCP4 and a 600-Å orthonormal grid. For each calculation, the Fourier transform of 60 unit cells was averaged and then plotted with GNUPLOT 4.0 (<http://www.gnuplot.info>).

RESULTS

LDLR-binding Activity of ApoE4•DPPC Particles—DPPC was chosen for structural studies because it has a relatively high transition temperature (41°C) and closely resembles physiological phospholipids. ApoE4•DPPC particles contain two molecules of apoE4 and 96 molecules of DPPC (23). The binding of these particles to the LDLR was determined in a competition assay with iodinated LDL and apoE•dimyristoylphosphatidylcholine (DMPC), a standard model system (19). These particles are biologically active and bind with high affinity to the LDLR (Fig. 1).

ApoE•DPPC, a Spheroidal Particle—The

diffraction pattern from the apoE4•DPPC crystals, flash cooled in liquid nitrogen, contained two distinct types of scattering: discrete Bragg peaks and diffuse scattering composed of rings and arcs (Fig. 2A). These diffuse scattering features are similar to the scattering observed from stacks of unoriented DPPC bilayers. In various hydration states, the scattering from DPPC bilayers typically contains an intense ring between 57.8 and 63.6 Å (27) and weaker rings between 4.0 and 4.5 Å (28). Flash-frozen DPPC bilayers prepared in the same buffer as the crystals displayed a sharp ring at 60.0 Å and two weaker rings at 4.24 Å and 4.08 Å (data not shown), suggesting that strong diffuse scattering from the apoE4•DPPC crystals is due to the DPPC molecules within the apoE4•DPPC particles.

In previous studies, the intense 60 Å ring was identified as a product of diffraction between two planes of phosphate atoms in adjacent bilayers (27). Similarly, the rings of diffuse scattering at 4.24 Å and 4.08 Å were associated with long-range order in the packing of the glycerohydrocarbon tails (28). In the apoE4•DPPC crystals, a sharp ring of high-intensity scattering was observed at 60.8 ± 0.3 Å, but the diffuse scattering centered on 4.2 Å was restricted to arcs rather than a complete ring (Fig 2A). The intensity of these features was independent of the crystal orientation with respect to the x-ray beam.

Only once did the intensity of the ring deviate significantly from the average intensity (Fig. 2B). This deviation is the result of secondary diffraction, since two large Bragg peaks overlap the ring in this orientation. Similarly, the intensity of the 4.2 Å arcs is nearly independent of crystal orientation.

This pattern of diffuse scattering is inconsistent with the prevailing models of disk-like particles, in which the central phospholipid molecules are arranged in a bilayer (29, 30). Using the particle position and orientation derived from the molecular replacement solution discussed below, the predicted diffuse scattering patterns of a disk 40 Å high and 30 Å in radius with short interatomic distances parallel to the b-axis was calculated. The resulting pattern had strong bands centered on the l-axis in the 0KL plane and the h-axis in the HK0 plane at 4.2 Å and 4.5 Å (Fig. 3B). The presence of the two bands is due to distribution of short distances in the model disks. (Fig. 3C and D). The scattering from the outer layers of the disk is limited to the HOL plane and shows up as distinct rings whose maxima follow the rule $40/N$, where N is an integer. Both the 4.2–4.5 Å

bands and the 40 Å ring are maximal in their respective planes, indicating that the predicted pattern of intensity for a bilayer within the crystal (Fig. 2C) is qualitatively correct. From this analysis, it is clear that the pattern of diffuse scattering from the apoE4•DPPC crystals does not originate from lipid arranged in a bilayer.

The diffuse scattering can be partially replicated by using similar calculations and a spherical model for the phosphate atoms 30 Å in radius filled with carbon atoms placed 4.2 Å apart with no preferred orientation. As expected, this calculation gives a family of spherical shells occurring at $60 \text{ Å}/N$, where N is an integer. Since analysis of the diffuse scattering cannot detect minor populations of DPPC molecules that deviate from the average 60.8 Å spacing between the phospholipid head groups, one cannot conclude that the particle is perfectly spheroidal. Therefore, the possible geometry of the DPPC particles derived from the diffuse scattering pattern most likely ranges from spherical to ellipsoidal.

Diffuse scattering due to the glycerohydrocarbon chains in a spheroidal model is more difficult to model. However, the results of the disk calculation suggests that the 4.2 Å arc in the diffraction pattern originates from a preferred orientation of a subset of the glycerohydrocarbon tails within the particle. Although there is insufficient information to model the packing of the phospholipid hydrocarbon chains, one explanation for a preferred orientation of a population of the glycerohydrocarbon chains is that the particle is slightly compressed into an ellipsoidal shape in a manner that leaves the majority of the phospholipid following an approximately spherical surface.

Therefore, the diffuse scattering observed from the apoE4•DPPC crystals is consistent with the diffuse scattering expected from a spheroidal particle rather than a particle containing a DPPC bilayer. This result is not simply due to rotational disorder within the crystal, since that would suggest that the apoE4•DPPC particles are rotationally disordered, which is incompatible with the presence of sharp Bragg reflections. Similarly, since the crystals readily dissolve into discrete particles similar in size to those used to form the crystals (23), the diffuse scattering from these crystals does not result from fusion of particles.

The parameters derived from the spheroidal model are consistent with the known packing parameters of DPPC. Arranging the phospholipid head groups are

on the surface of a spherical shell 60.8 Å in diameter predicts an average length of 30.4 Å for the DPPC molecules, a value well within the range of estimated lengths of DPPC molecules in DPPC bilayers at low temperature.

If the particle is approximated as a sphere, the specific molecular volume of the DPPC glycerohydrocarbon tails is 832–1225 Å³/molecule. For comparison, the specific molecular volume of the glycerohydrocarbon tails of DPPC is estimated to be 1063 Å³/molecule at 24°C (28), or about 946 Å³/molecule after allowing for thermal contraction when the crystals are cooled to 140 K. Owing to the curvature of the spherical surface, the estimated surface area per DPPC head group, 78–120 Å², is higher than the corresponding measurements of 48–71 Å²/molecule observed for DPPC bilayers at temperatures greater than 273 K. However, similar molecular volumes and an unusually large measured surface area per head group were observed in rippled phases of DPPC, in which excess space between the polar head groups is filled with solvent molecules (31). Analogous packing most likely exists in apoE4•DPPC particles, with solvent filling the surface gaps between the polar heads groups and, closer to the center, the folded glycerohydrocarbon tails forming a tightly packed core.

The spheroidal shape of the apoE4•DPPC particles was unexpected because negative-staining electron microscopy of dehydrated samples suggested disk-shaped particles with approximate dimensions of 60 Å by 80 Å (23), consistent with previous models. However, since the crystals are approximately 60% solvent by volume, the hydration state could easily account for the difference.

As shown in (23), different concentrations of cholate and lipid to protein ratios during purification result in a family of apoE4•DPPC particles with different electrophoretic mobilities, most likely resulting from variations in shape and size. Analysis of the diffuse scattering indicates that the purification process and the lipid to protein to cholate ratios we used select for LDLR-active spheroidal particles. Whatever the fine details of the lipid arrangements, the spheroidal pattern of diffuse scattering indicates that the phospholipid does not form a bilayer as predicted by previous models of DMPC-containing particles. Instead the phospholipid is randomly oriented within the unit cell and therefore contributes minimally to the Bragg diffraction.

Lipid-Bound ApoE Forms a Helical Hairpin—The

choice of these particular particles for crystallization was serendipitous, since the random orientation of the lipid implies that the Bragg peaks must result primarily from diffraction by the protein atoms. This presented a unique opportunity to solve the structure of the molecular envelope of apoE by molecular replacement. Two models of apoE bound to DMPC particles have been proposed: the “picket fence” and “belt” models (29, 30). In the picket fence model, apoE is folded into a series of short, 21-residue helices wrapped around the edge of a discoidal bilayer, with the helices approximately parallel to the hydrocarbon chains. In the belt model, apoE is folded into a single continuous helix that wraps around the disc, with the helix perpendicular to the exposed hydrocarbon chains of the phospholipid. At 10 Å resolution, the picket fence model predicts a curved band of protein approximately 10 Å deep and wide, whereas the belt model predicts a complete ring of protein 10 Å deep and 20 Å wide. Because the self-rotation function indicated two twofold rotation axes in the apoE4•DPPC crystals (see Supplementary Information), it is unlikely that apoE forms a ring that completely encircles the particle. Therefore, models describing fractions of a ring were used in a molecular replacement search.

Each search model was generated by placing pseudoatoms at a constant density within an envelope defined by five parameters: height, radius, width, angle circumscribed by the belt, and eccentricity (Fig. 4A). For each combination (>10,000), the molecular replacement solution was determined. The correlation coefficient and R-factor of each solution depended strongly on the height, width, and eccentricity of the belt. For each value of the radius and angle, the optimal parameters were 20.0 ± 1 Å for height, 9.5 ± 1 Å for width, and 1.0 ± 0.02 Å for eccentricity. A value of a 1.0 for the eccentricity indicates that the optimal model has a nearly perfect spherical cross-section. Solutions can be obtained for different values of the radius and angle with relatively high correlation coefficients. However, to obtain a solution that closely matches the self-rotation function with good packing, the value of the outer radius is restricted to a range of 42 ± 1 Å, and the angle of completeness to $310 \pm 10^\circ$. The correlation coefficients for this family of solutions were 0.76–0.79, and the R-factors were 0.46–0.50 for all reflections between 50 and 10 Å. At first, it might seem counterintuitive that 10 Å data specify the dimensions of the envelope parameters with such accuracy. However, altering

any one of the parameters induced changes in the Patterson search vectors in the range of 10–80 Å.

The resulting molecular envelope was an incomplete toroid that resembles a horseshoe with a circular cross-section in the equatorial plane (Fig. 4A). The noncrystallographic twofold rotation axis generated a second horseshoe-shaped envelope that faces the first in an orientation that clearly suggested that the surface of the particle is spheroidal (Fig. 4B), consistent with the diffuse scattering analysis. In this model, the apoE molecules would project beyond the surface of the phospholipid head groups with an outer diameter between the envelopes of 84 ± 2 Å, which correlates with the maximum dimension of the dehydrated particles estimated by negative-staining electron microscopy (23). The envelopes form the primary crystal contacts, but the overlaps between adjoining envelopes are restricted to 3–4 Å, which is well within the expectation at this resolution.

Although 10 Å resolution is insufficient to distinguish the secondary structure inside the envelope, the optimal width (9.5 Å) and height (20 Å) match the dimensions of the electron density resulting from a side-by-side pair of helices at 10 Å resolution, such as the helices in the apoA-II crystal structure (32). This suggests each apoE molecule can be approximated as a pair of extended helices folded into a semicircular arc and stacked one on top of the other. However, since circular dichroism spectroscopy estimated that the helical content of apoE is 64% in DPPC particles but only 53% in the lipid-free protein, the molecular envelope likely contains a series of short helices and connecting loops (Fig. 5A).

Interaction with Phospholipid Head Groups—Comparison of the distance between the phosphate atoms derived from powder diffraction and the optimal dimensions of the protein envelope derived from molecular replacement suggested that a significant fraction of the volume of the apoE molecule ($\approx 42\%$) projects beyond the surface of the phospholipid head groups. Since the hydrophobic environment of the DPPC particle did not begin until 5–9 Å below the phosphate atoms, depending on the phase (31), the estimate of the inner radius of the toroid (22 Å) matches the approximate edge of the hydrocarbon core of the particle (Fig. 5B). Therefore, the majority of the apoE's surface residues face either the DPPC glycerol oxygens, the polar phospholipid head groups, the solvent molecules trapped between the phospholipids, or the

exterior solvent.

To be favorably folded into this predominately hydrophilic environment, the tertiary structure of apoE most likely resembles the structure apoA-I (33) or of apoA-II in the presence of detergent (32). In both of these models, the proteins are composed of long curved helices with a superhelical twist. This conclusion is in sharp contrast to the prevailing models of how apoE binds to lipid. In other models, the majority of the hydrophobic residues of apoE interact with the glycerohydrocarbon tails (29, 30). However, much of the work supporting these models used an N-terminal fragment of apoE and DMPC. Thus, the different size, composition, and presence of the C-terminal domain on the apoE4•DPPC particles may account for the differences.

Helical Hairpin Model of ApoE—The simplest way to accommodate apoE within the incomplete toroid is to fold the molecule in half to create a helical hairpin similar to detergent-associated apoA-II. This conformation would satisfy the symmetry of the molecular envelope, as each arm of the toroid would contain approximately half the residues in apoE. The radial dimension of the molecular envelope is consistent with two extended helices of approximately 130 residues, which matches the length of the N-terminal four-helix bundle (residues 24–160). Based on these parameters, a helical hairpin model of apoE can be built that is consistent with the helical content measured by circular dichroism (64%), the observed secondary structure of the N-terminal domain, and the predicted secondary structure of the C-terminal domain (15–17). From the modeling, one superhelical twist is required to keep within the confines of the molecular envelope and maintain good geometry. The C-terminal domain contributes more to the buried surface than the N-terminal domain to increase the accessibility of the residues in the LDL receptor-binding site. This orientation is consistent with two prior observations: (1) that the association with phospholipid masks the thrombin cleavage site at residue 191 and the C-terminal heparin binding site (34) and (2) that the C-terminal domain initiates the binding of apoE to DMPC and has a higher avidity for lipid than the N-terminal domain (35).

Using a helical hairpin model (Fig. 5A) for molecular replacement gave the same solution as the optimal molecular envelope with a correlation coefficient of 0.78 and a crystallographic R-factor of 0.46. Addition of a spherical shell of 96 randomly distributed phosphate atoms lowered the

crystallographic R-factor to 0.43 and increased the correlation coefficient to 0.83. Finally, filling in the spherical shell of phosphate atoms with a sphere of randomly distributed carbon atoms lowered the crystallographic R-factor to 0.39 and increased the correlation coefficient to 0.85.

The molecular envelope at 10 Å resolution does not by itself uniquely determine the protein structure. A helical hairpin structure could result from a number of different permutations of smaller helices and loops within each arm of the hairpin. Similarly, the extent of the super helical twisting between the arms cannot be determined. Finally, segments of the N-terminal and C-terminal domains could be intermixed in some more complicated superstructure. However, it is difficult to envision the driving force that would cause such complicated structural rearrangements, when the molecule could simply fold in half. A higher-resolution structure will be required to address this possibility.

The LDLR-Binding Site Is at the Apex of the Hairpin—Placing the apex of the helical hairpin near the end of the N-terminal bundle brought all the known elements of the LDLR binding site into close proximity (Fig. 6A) (13, 36). In lipid-free apoE, the residues at the end of the fourth helix of the N-terminal domain (residues 140–160) and arginine 172 in the loop connecting the two domains are separated by more than 15 Å. When residues 160–170 were modeled as the apex loop, arginine 172 (at the beginning of the first helix of the C-terminal domain) was adjacent to the end of the last helix of the N-terminal domain, helix 4. In the model, arginine 172 was close to the other required residues on helix 4 (arginines 134, 142, and 145) (Fig. 6A). Thus, the helical hairpin model directly explains why lipid association is required for high-affinity binding of apoE to the LDLR.

The assignment of residues 160–170 to the apex loop is supported by previous analysis of the biological activity and structure of fragments of apoE. Truncation of apoE at residue 165 abolishes receptor-binding activity, but apoE truncated at residue 191 is receptor-active (37). In addition, locating the turn after residue 150 preserves the secondary structure of residues 130–150. Preservation of the helical character of these residues is an important constraint on the model, since the 1D7 and 2E8 monoclonal antibodies, whose epitopes include these residues, recognize both lipid-free and lipid-associated apoE (38). Finally, NMR analysis of residues 126–183 bound to

dodecylphosphocholine micelles indicated that this fragment consists of one long extended helix with a pronounced bend beginning at residue 151 (39) and continuing through residue 170. Residue 151 is also the location of a kink in helix IV in the lipid-free crystal structures of the N-terminal domain (40). The degree and orientation of this kink vary in different crystal forms, suggesting that the conformation of residues C-terminal to arginine 150 depends highly on their environment.

The pattern of residues 160–170 also indicates that they likely form a turn. Half are alanines or glycines, a unique occurrence within the apoE sequence. In the lipid-free structures, residues 164–171 are disordered, suggesting flexibility. Along with the polar residues in this region, this cluster of small residues is conserved across species. The sequence conservation, combined with the biological activity and structure of various apoE fragments, is consistent with a model in which residues 150–172 form the connecting turn between the two extended helices.

The hairpin model includes a possible role for this cluster of small flexible residues. In the model, glycines 165 and 169 are critical in forming the tight connecting turn. Although there are many ways to build the turn, at least one of the residues must adopt a *cis*-conformation to keep the turn within the envelope and bring arginine 172 into juxtaposition with the rest of the residues implicated in LDLR binding (Fig. 6). Indeed, the LDLR may recognize a specific conformation of this loop. Thus, the hairpin structure induced by binding to DPPC explains why apoE must be lipid bound to bind with high affinity to the LDLR within the constraints of the molecular envelope.

In summary, analysis of the diffraction of apoE4•DPPC crystals demonstrates that the particles are spheroidal with a diameter of 60.8 Å between the phosphate atoms of the phospholipid head groups. The molecular envelope of apoE is an incomplete toroid. Two extended helices, representing the N- and C-terminal domains, are stacked and packed so that most of the hydrophobic residues in the helices form an interface between the two extended helices rather than interacting with the hydrophobic core of the particle. Modeling of apoE as a helical hairpin fits well within the molecular envelope and creates a distribution of polar and hydrophobic residues such that apoE interacts primarily with the DPPC phospholipid head groups and glycerol oxygens. Finally, the crystallographic symmetry and the

results of previous mutagenesis and structural studies indicate that the LDLR binding site is either adjacent to or part of the turn at the apex of the helical hairpin and that the formation of this hairpin loop resulting from lipid association is critical for high-affinity LDLR binding activity.

Acknowledgments—The work would not have been possible without generous grants of synchrotron time through the general user programs of the Advanced Light Source, Lawrence Berkeley National Laboratory, and the Stanford Synchrotron Radiation Laboratory. The authors thank Drs. Keith Henderson, Ron Stenkamp, Donald Small, Graham Shipley, Olga Gursky, and Corie Ralston for helpful discussions about data collection and interpretation; Karina Fantillo for manuscript preparation; John Carroll, Jack Hull, and Stephen Gonzales for graphics preparations; and Stephen Ordway and Gary Howard for editorial assistance.

REFERENCES

- Segrest, J. P., Jones, M. K., De Loof, H., and Dashti, N. (2001) *J. Lipid Res.* **42**, 1346–1367
- Mahley, R. W. (1988) *Science* **240**, 622–630
- Weisgraber, K. H., and Mahley, R. W. (1996) *FASEB J.* **10**, 1485–1494
- Saunders, A. M., Strittmatter, W. J., Schmechel, D., St George-Hyslop, P. H., Pericak-Vance, M. A., Joo, S. H., Rosi, B. L., Gusella, J. F., Crapper-MacLachlan, D. R., Alberts, M. J., Hulette, C., Crain, B., Goldgaber, D., and Roses, A. D. (1993) *Neurology* **43**, 1467–1472
- Corder, E. H., Saunders, A. M., Strittmatter, W. J., Schmechel, D. E., Gaskell, P. C., Small, G. W., Roses, A. D., Haines, J. L., and Pericak-Vance, M. A. (1993) *Science* **261**, 921–923
- Strittmatter, W. J., and Roses, A. D. (1995) *Proc. Natl. Acad. Sci. U. S. A.* **92**, 4725–4727
- Mayeux, R., Ottman, R., Maestre, G., Ngai, C., Tang, M.-X., Ginsberg, H., Chun, M., Tycko, B., and Shelanski, M. (1995) *Neurology* **45**, 555–557
- Slooter, A. J. C., Tang, M.-X., van Duijn, C. M., Stern, Y., Ott, A., Bell, K., Breteler, M. M. B., Van Broeckhoven, C., Tatemichi, T. K., Tycko, B., Hofman, A., and Mayeux, R. (1997) *J. Am. Med. Assoc.* **277**, 818–821
- Fazekas, F., Strasser-Fuchs, S., Schmidt, H., Enzinger, C., Ropele, S., Lechner, A., Flooh, E., Schmidt, R., and Hartung, H.-P. (2000) *J. Neurol. Neurosurg. Psychiatry* **69**, 25–28
- Drory, V. E., Birnbaum, M., Korczyn, A. D., and Chapman, J. (2001) *J. Neurol. Sci.* **190**, 17–20
- Davignon, J., Gregg, R. E., and Sing, C. F. (1988) *Arteriosclerosis* **8**, 1–21
- Eichner, J. E., Dunn, S. T., Perveen, G., Thompson, D. M., Stewart, K. E., and Stroehla, B. C. (2002) *Am. J. Epidemiol.* **155**, 487–495
- Weisgraber, K. H. (1994) *Adv. Protein Chem.* **45**, 249–302
- Weisgraber, K. H. (1990) *J. Lipid Res.* **31**, 1503–1511
- Nolte, R. T., and Atkinson, D. (1992) *Biophys. J.* **63**, 1221–1239
- Segrest, J. P., Jones, M. K., De Loof, H., Brouillette, C. G., Venkatachalapathi, Y. V., and Anantharamaiah, G. M. (1992) *J. Lipid Res.* **33**, 141–166
- Aggerbeck, L. P., Wetterau, J. R., Weisgraber, K. H., Wu, C.-S. C., and Lindgren, F. T. (1988) *J. Biol. Chem.* **263**, 6249–6258
- Wilson, C., Wardell, M. R., Weisgraber, K. H., Mahley, R. W., and Agard, D. A. (1991) *Science* **252**, 1817–1822
- Innerarity, T. L., Pitas, R. E., and Mahley, R. W. (1979) *J. Biol. Chem.* **254**, 4186–4190
- Lu, B., Morrow, J. A., and Weisgraber, K. H. (2000) *J. Biol. Chem.* **275**, 20775–20781
- Morrow, J. A., Arnold, K. S., and Weisgraber, K. H. (1999) *Protein Expr. Purif.* **16**, 224–230
- Matz, C. E., and Jonas, A. (1982) *J. Biol. Chem.* **257**, 4535–4540
- Newhouse, Y., Peters-Libeu, C., and Weisgraber, K. H. (2005) *Acta Crystallogr. F* (submitted)
- Kabsch, W. (1993) *J. Appl. Crystallogr.* **26**, 795–800
- Hammersley, A. (2004) The Fit2D home page. <http://www.esrf.fr/computing/scientific/FIT2D/>. Accessed April 10, 2004.
- Vagin, A., and Teplyakov, A. (2000) *Acta Crystallogr. D* **56**, 1622–1624
- McIntosh, T. J., and Simon, S. A. (1986) *Biochemistry* **25**, 4058–4066
- Small, D. M. (1986) *The Physical Chemistry of Lipids. From Alkanes to Phospholipids*, eds, pp. 512–517, Plenum Press, New York
- De Pauw, M., Vanloo, B., Weisgraber, K., and Rosseneu, M. (1995) *Biochemistry* **34**, 10953–10960
- Raussens, V., Fisher, C. A., Goormaghtigh, E., Ryan, R. O., and Ruyschaert, J.-M. (1998) *J. Biol. Chem.* **273**, 25825–25830
- Nagle, J. F., and Tristram-Nagle, S. (2000)

- Biochim. Biophys. Acta* **1469**, 159–195
32. Kumar, M. S., Carson, M., Hussain, M. M., and Murthy, H. M. K. (2002) *Biochemistry* **41**, 11681–11691
 33. Borhani, D. W., Rogers, D. P., Engler, J. A., and Brouillette, C. G. (1997) *Proc. Natl. Acad. Sci. U. S. A.* **94**, 12291–12296
 34. Weisgraber, K. H., Rall, S. C., Jr., Mahley, R. W., Milne, R. W., Marcel, Y. L., and Sparrow, J. T. (1986) *J. Biol. Chem.* **261**, 2068–2076
 35. Segall, M. L., Dhanasekaran, P., Baldwin, F., Anantharamaiah, G. M., Weisgraber, K. H., Phillips, M. C., and Lund-Katz, S. (2002) *J. Lipid Res.* **43**, 1688–1700
 36. Morrow, J. A., Arnold, K. S., Dong, J., Balestra, M. E., Innerarity, T. L., and Weisgraber, K. H. (2000) *J. Biol. Chem.* **275**, 2576–2580
 37. Lalazar, A., Ou, S.-H. I., and Mahley, R. W. (1989) *J. Biol. Chem.* **264**, 8447–8450
 38. Raffai, R., Maurice, R., Weisgraber, K., Innerarity, T., Wang, X., MacKenzie, R., Hiram, T., Watson, D., Rassart, E., and Milne, R. (1995) *J. Lipid Res.* **36**, 1905–1918
 39. Raussens, V., Slupsky, C. M., Sykes, B. D., and Ryan, R. O. (2003) *J. Biol. Chem.* **278**, 25998–26006
 40. Segelke, B. W., Forstner, M., Knapp, M., Trakhanov, S. D., Parkin, S., Newhouse, Y. M., Bellamy, H. D., Weisgraber, K. H., and Rupp, B. (2000) *Protein Sci.* **9**, 886–897
 41. Pitas, R. E., Innerarity, T. L., Arnold, K. S., and Mahley, R. W. (1979) *Proc. Natl. Acad. Sci. U. S. A.* **76**, 2311–2315

FOOTNOTES

*This work was supported in part by Grant HL-64963 from the National Institutes of Health (to K.H.W.).

**To whom correspondence should be addressed. Tel.: 415-734-2000; Fax: 415-355-0824; E-mail: kweisgraber@gladstone.ucsf.edu.

¹The abbreviations used are: apo, apolipoprotein; LDL, low density lipoprotein(s); LDLR, LDL receptor; DPPC, dipalmitoylphosphatidylcholine; DMPC, dimyristoylphosphatidylcholine.

FIGURE LEGENDS

FIG. 1. **LDLR binding of apoE•DMPC and apoE4•DPPC complexes.** Increasing concentrations of complexes were examined for their ability to compete with ¹²⁵I-LDL (2 µg/ml) for binding to

LDLRs on cultured fibroblasts. Since the number of apoE molecules per phospholipid particle influences the LDLR binding activity, the apoE•DPPC particles with two apoE molecules per particle are expected to have a lower binding activity than apoE•DMPC particles, which have four apoE molecules per particle (41).

FIG. 2. **Diffuse scattering from apoE4•DPPC crystals.** *A*, a representative 0.25° oscillation photo of an apoE4•DPPC crystal cropped so that the outer edge of the pattern is at 2.7 Å. The inset shows a companion 1° oscillation photo cropped at 40 Å in which the lower-resolution Bragg peaks and 60.8 Å ring are resolved; the Bragg peaks overlap because of the long exposure time necessary to obtain good counting statistics for the ring. *B*, intensity of the diffuse scattering features as a function of crystal orientation. The peak intensity of the 60.8 Å ring (*dotted line*) and the 4.2 Å arcs (*solid line*) were obtained with the program Fit2D (25) from 0.25° oscillation images. For comparison, each curve was normalized by dividing by the twice the standard deviation of each series: 30/pixel for the 4.2 Å arcs and 100/pixel for the 60.8 Å ring. Representative oscillation images from this crystal are presented in the Supplementary Material. *C*, predicted pattern of diffuse scattering for a disk containing a DPPC bilayer. Variation of the peak intensity of the 60 Å ring (*dotted*) and 4.2 Å arcs (*solid*) with crystal orientation for a crystal composed of disks containing DPPC bilayers stacked so that the layers of the phospholipid head groups are perpendicular to the b-axis. This figure assumes that the b-axis of the crystal lattice is perpendicular to the rotation axis of the crystal.

FIG. 3. **Predicted scattering from two model disks, 40 Å in height and 30 Å in radius related by the crystallographic symmetry operation.** The bilayer is oriented parallel to the b-axis. *A*, H0L plane. *B*, 0KL plane. *C*, the distribution of difference vectors with the core of the disk. *D*, the distribution of the orientation of the difference vectors between 3.5–5.0 Å with respect to the b-axis.

FIG. 4. **Molecular replacement model.** *A*, the best molecular replacement model was an incomplete toroid with an outer radius of 42 Å, an angle of completeness (ω) of 310°, a height of 20.0 Å, a width of 9.5 Å, and an eccentricity of 1.0. *B*, packing diagram of the Van der Waals surface of the incomplete toroids. The noncrystallographic twofold

axis relates each pair of molecules within one layer. For example, the dark cyan pair, the light cyan pair, and each dark-light pair are related by combinations of the noncrystallographic twofold axis and a cell translation. The cyan layer and the green layer are related by the crystallographic twofold screw axis. The packing of the molecules is consistent with the diffuse scattering data, since the largest area that can accommodate the glycerohydrocarbon tails of the DPPC molecule is contained within a region that is symmetric about an axis parallel to the crystallographic twofold screw axis. This orientation is consistent with the arc-like appearance of the diffuse scattering from the glycerohydrocarbon tails.

FIG. 5. Models of apoE-DPPC. *A*, relationship of the incomplete toroid to the molecular model. The surface of the incomplete toroid is shown in *gray*. The molecular model is colored to show the known secondary structure of the N-terminal domain: helix I in *red*, helix II in *blue*, helix III in *green*, and helix IV and the connecting loop in *yellow*. The residues that contribute to the LDLR binding site are in *light yellow*. The residues of the C-terminal domain are shown in *gray*. Although the dimensions of the incomplete toroid limit the molecule to pairs of helices, several different models are possible, depending on how the loops connecting the helices are modeled. For example, if the loop between helix I and II of the N-terminal domain is allowed to loop out, then most of the residues of the LDL-receptor binding site can be accommodated in the envelope. Similarly, extension of the incomplete toroid from 310° to 320° also accommodates all of the molecular model within the envelope. *B*, A cartoon of the cross-section of an apoE4-DPPC particle. The *light blue circle* in the center represents the tightly packed core composed of DPPC glycerohydrocarbon tails. The *gray area* represents the less tightly packed hydrophilic crust of the particle. This region results from the interdigitation of solvent molecules between the polar head groups. The head groups of the phospholipids are shown in *red*, and a cross-section of each apoE molecule (*A* and *B*) is shown in *purple*.

TABLE I

Data statistics for apoE•DPPC.

	All reflections ^a		Strong reflections ($I/\sigma(I) > 3.0$) ^b	
	50–10 Å	12.5–10 Å	50–10 Å	12.5–10 Å
Completeness	99%	100%	83%	71%
R_{merge}^c	6.2%	21%	4.0%	11.8%
Redundancy	3.5	3.4	3.5	3.5
$\langle I/\sigma(I) \rangle^d$	22	6.3	18	5.3

^aThe total number of reflections that were observed was 3,063 with 881 unique reflections.

^bThe total number of strong reflections was 2,449 with 745 unique reflections.

^c $R_{\text{merge}} = \sum_{ij} (\langle I_i \rangle - I_{ij})^2 / \sum_i \langle I_i \rangle$, where $\langle I_i \rangle$ is the average intensity of the i^{th} reflection and I_{ij} is the intensity of the j^{th} observation of the i^{th} reflection.

^d I is the intensity of the reflection and $\sigma(I)$ is its estimated error.

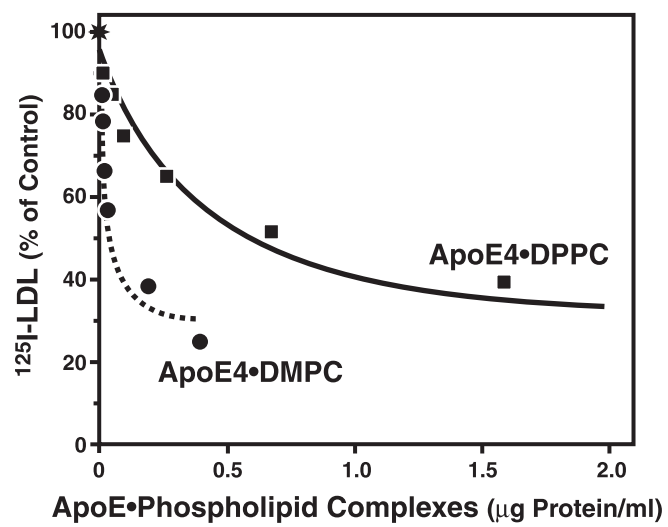


Figure 1

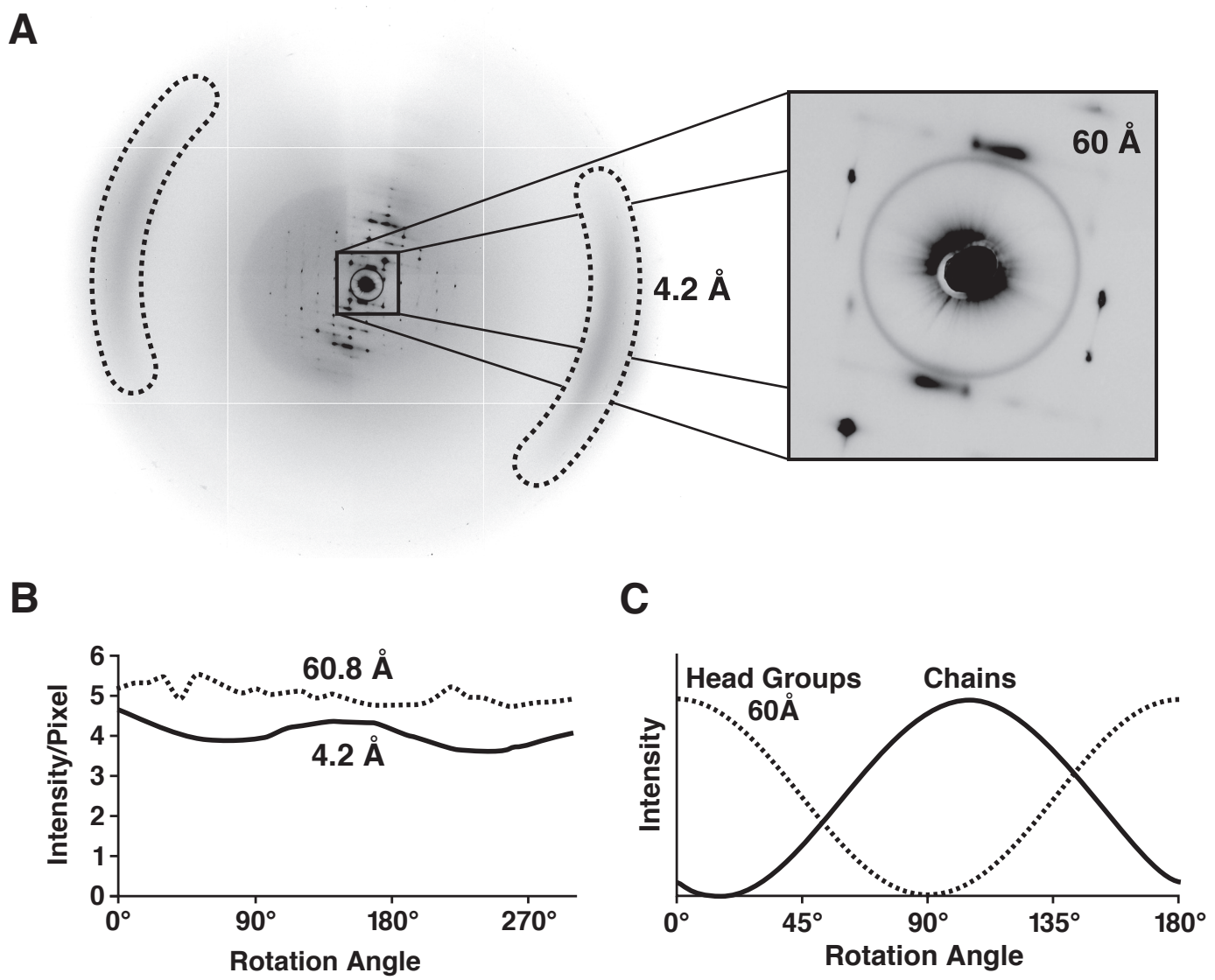


Figure 2

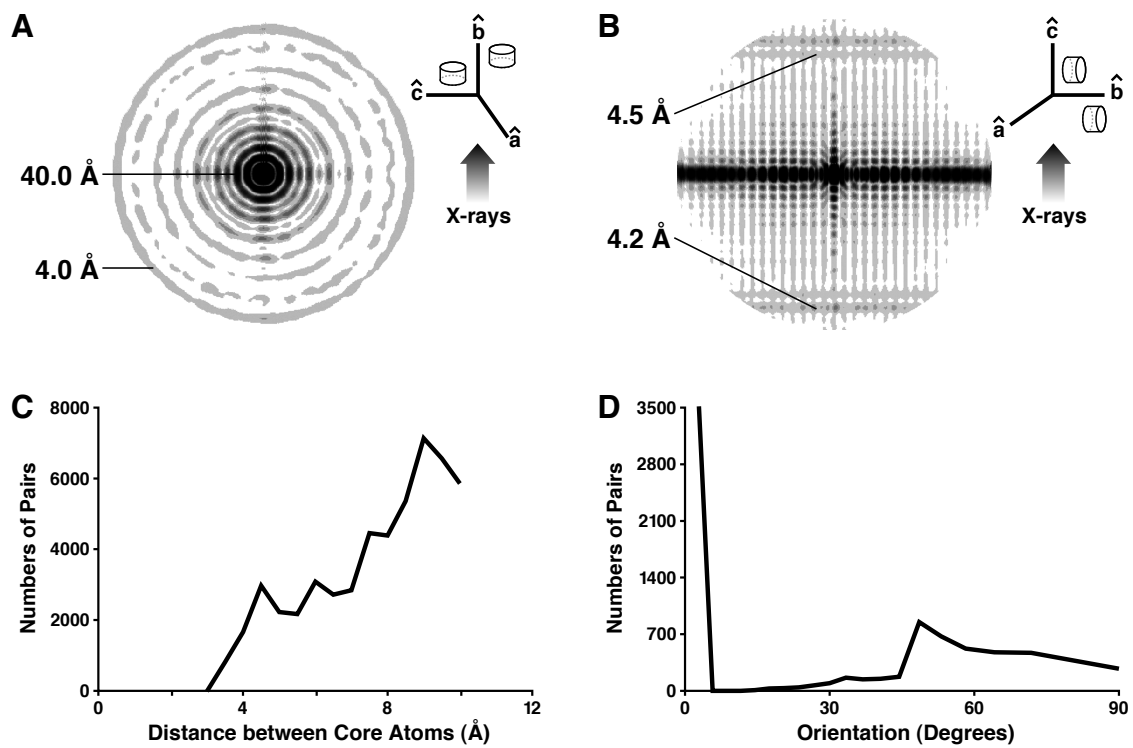
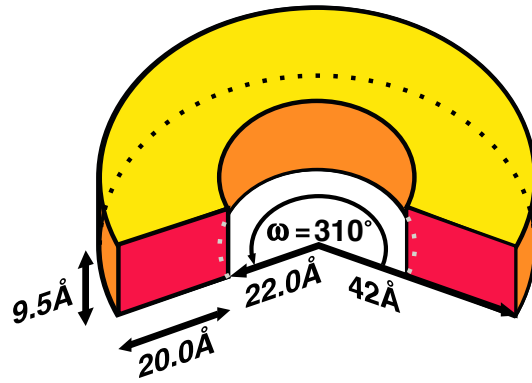


Figure 3

A



B

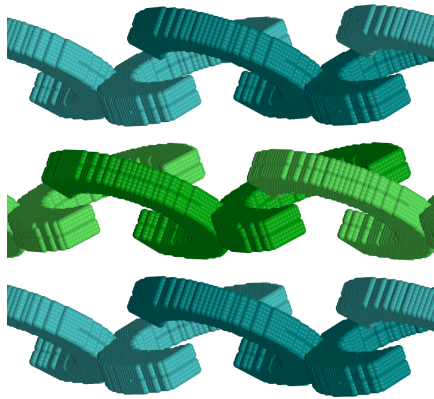


Figure 4

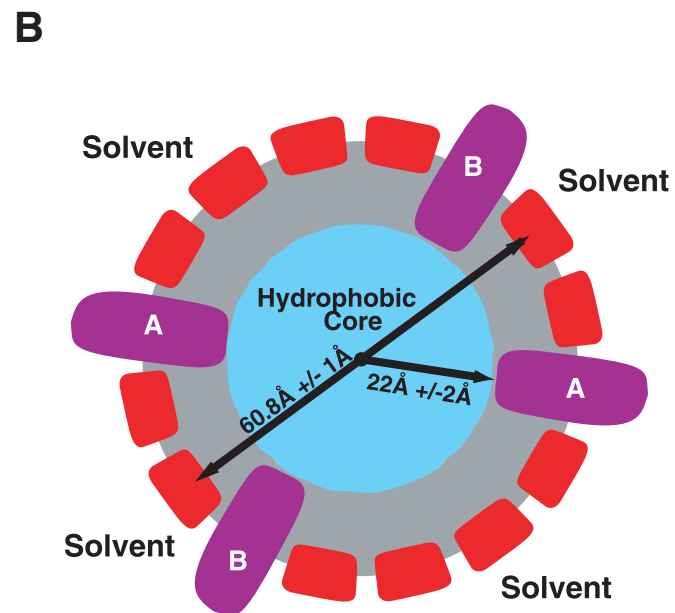
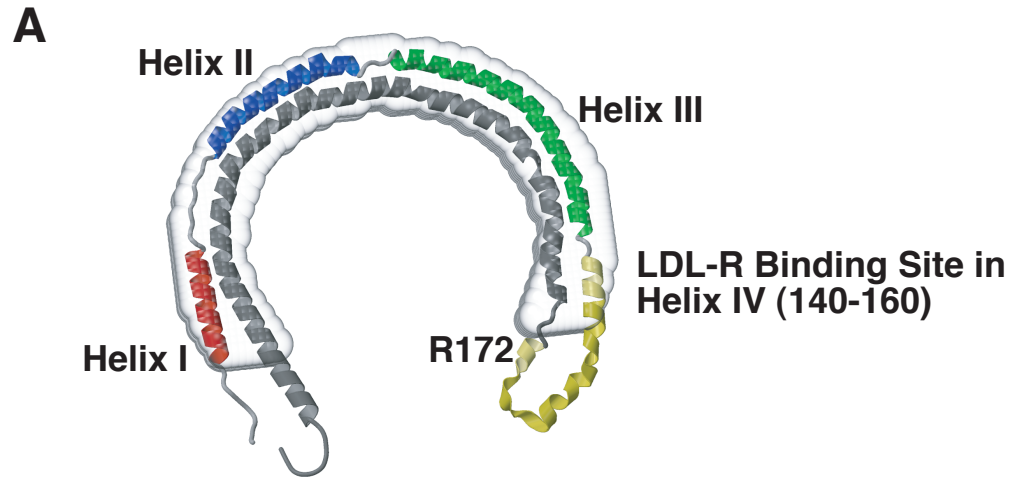


Figure 5